

A Generalized Distance Transform: Theory and Applications to Weather Analysis and Forecasting

Dominique Brunet and David Sills

Abstract—The distance transform (also known as distance map or distance field) is a fundamental tool of mathematical morphology. We introduce a Generalized Distance Transform (GDT) that is smoother than the classical distance transform. This transform can be used to define a generalized Hausdorff metric that is shown to be more robust to noise while preserving all metric properties. It is also shown to lead to smoother level sets, allowing contour evolution without having to solve a Partial Differential Equation (PDE). Two applications in weather analysis and forecasting demonstrate the usefulness of this proposed GDT. Specifically, the dilation of sets according to the GDT allows the simplification of numerical weather forecasts and analysis into geometric objects, called MetObjects, and the generalized Hausdorff distance can be used as a forecast verification metric.

Index Terms—Distance transform, Hausdorff distance, level-set methods, meteorological applications, MetObject, object-based distance, shape processing.

I. INTRODUCTION

Mathematical morphology [1] has been proven to be a useful tool for the analysis of remotely sensed images. Dilation and erosion, the basic operations in mathematical morphology, are used to modify the boundary of an object in a binary image by adding or removing pixels from the object. A distance transform (DT) can then be introduced to measure the change in binary images as a function of the number of dilations applied. The contour of the distance transform of a binary image at an integer value n is equivalent to the boundary of n successive dilations of the same binary image. The distance transform generalizes the dilation operator as a continuous dilation, made possible by choosing a real value for the contouring operation. This can be thought of as representing a curve evolution with a constant unit speed. If we assign negative values for the distance transform of the complement of the binary image, then the so-called signed distance transform also generalizes the erosion operator.

The Hausdorff distance between two sets can be readily computed from their distance transforms. Contrary to contingency-based scores such as Probability of Detection (POD), False Alarm Rate (FAR) and Threat Score (TS), the Hausdorff distance depends on the magnitude of translation between two sets even when the sets do not intersect.

Distance transforms find broad application in fluid dynamics, industrial design, geoscience, medical imaging, image processing and computer vision (see [2], [3]). Many different algorithms use the distance transform in order to simplify

binary images (e.g. skeletonization [4], grouping, noise reduction [5]). Also, the initialization of popular level set methods (LSM) relies on a signed distance transform (see [2], [6]). Furthermore, the ubiquitous Hausdorff distance is based on the distance transform [7]. Finally, some shape matching and morphing techniques rely on an implicit representation of contours obtained from the distance transform [8], [9].

Distance transforms, morphological operations and Hausdorff distance are also commonly used in the field of remote sensing (see [10], [11]). For example, it has been used in an image retrieval system [12], for image segmentation and classification [13], [14], for image quality control [15] and for validation of image segmentation algorithms [16].

One undesirable feature of the distance transform is that it is not differentiable everywhere when applied on a non-convex set. In fact, as seen in Fig. 1(a), kinks appear for points in the ambient space which have two or more nearest points on the set on which the distance transform is computed. In the implementation of contour evolution using level set methods this might have no negative impact, since smoothing occurs anyway in the computation. However, for morphological operations this will lead to a shape that is less smooth than the original, something that is generally unwanted.

Another undesirable feature of the distance transform is its lack of robustness in the treatment of outliers. This is the direct cause of the same well-known weakness of the Hausdorff distance. Some authors have attempted to modify the Hausdorff distance to make it more robust to outliers, but the metric property of the distance is generally lost in the process [17], [18].

An exception is Baddeley's Delta-metric [19] which naturally extends the Hausdorff distance into a more robust metric based on the L^p -norm. However, we will show that even this extension can be sensitive to outliers.

We propose a generalized distance transform (GDT) that is smoother and more robust in the treatment of outliers (see Fig. 1). This new distance transform replaces the minimum by a generalized mean with a negative exponent. The impact of this change is that all points in the set influence the value of the distance transform at one location, but points closer to this location will have more weight. This is in contrast with the classic distance transform that allocates all the weight to the nearest point. Combined with Baddeley's Delta-metric, this distance transform is shown to lead to a robust distance metric for sets.

Definitions of the GDT and of the associated metric will be carried on in Section II. Sections III and IV will respectively study the smoothness of the distance transform and the ro-

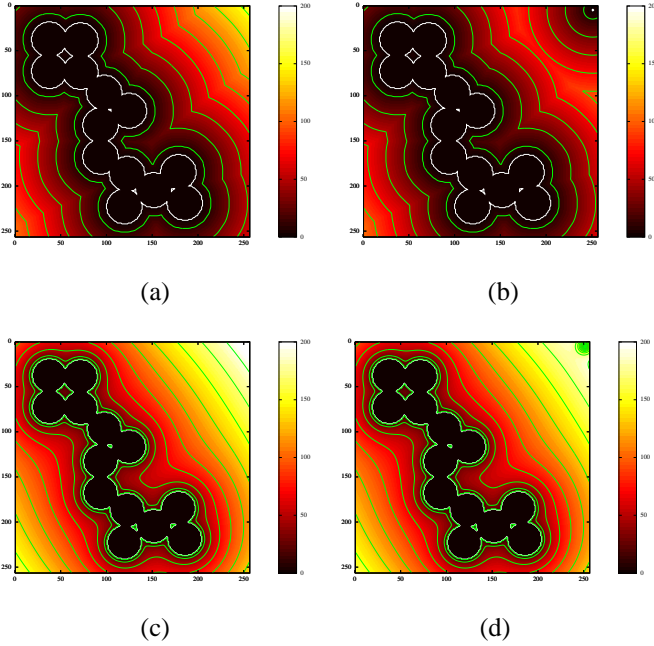


Fig. 1. Computation of the distance transform. The black disks with white boundaries are the set on which the distance transform is computed. A 'hot' colour map indicates the distance from each pixel location. Green contours at regular intervals are also shown for each distance transform. (a) The classical distance transform. (b) The classical distance transform with a single outlier. (c) The generalized distance transform with a single outlier. Notice the difference in smoothness and the different effect of the outlier between the classical and the generalized distance transform.

bustness of the associated distance. Applications for computer-aided weather forecasting will be demonstrated in Section V. Concluding remarks will wrap up this paper in Section VI. Details on the implementation of the GDT will be shown in the Appendix.

II. THEORY

A. Definitions and Properties

We introduce the (signed) distance transform and generalize it. The distance transform of a set $A \subset X$ is a function that measures the distance between any point x in the space X to the nearest point of the set A .

Let X be set with associated metric d , e.g. the Euclidean metric space. The Euclidean distance corresponds to the metric induced by the L^2 -norm. Other possibilities for point-to-point distances are the Manhattan (or city-block) distance and chessboard distance which correspond to, respectively, L^1 and L^∞ -induced metrics. The (classical) distance transform of $A \subset X$ at $x \in X$ is

$$D(x, A) := \inf_{a \in A} d(x, a), \quad (1)$$

where \inf is the infimum. If A is a closed subset of X (i.e. if it contains its own boundary), then the infimum can be replaced by a minimum.

The distance transform is zero for $x \in A$ and increases moving farther away from A . It is often convenient to introduce a

signed distance transform that takes negative values inside A :

$$\phi(x) = \begin{cases} D(x, A) & \text{if } x \in A^C, \\ -D(x, A^C) & \text{if } x \in A. \end{cases},$$

where A^C denotes the complement of A . This gives an implicit representation of a contour as the zero level set of a function $\phi(x)$. Indeed,

$$\begin{aligned} \phi(x) &= 0 && \text{for } x \text{ on the boundary of } A, \\ \phi(x) &< 0 && \text{for } x \text{ in the interior of } A, \\ \phi(x) &> 0 && \text{for } x \in A^C. \end{aligned}$$

We generalize the distance transform by changing the infimum operator by a power mean. For discrete and finite sets of positive real numbers $Y = (y_1, \dots, y_N)$, the power mean is defined as

$$M_q(Y) = \left(\frac{1}{N} \sum_{n=1}^N y_n^q \right)^{1/q} \quad (2)$$

for $-\infty \leq q \leq \infty$. The cases $q = -\infty$, $q = 0$ and $q = \infty$ are understood as their respective limits. Thus, we have

$$\begin{aligned} M_{-\infty}(Y) &= \min_{1 \leq n \leq N} y_n, \\ M_\infty(Y) &= \max_{1 \leq n \leq N} y_n, \\ M_0(Y) &= \prod_{1 \leq n \leq N} y_n^{1/N}, \end{aligned}$$

where \prod represents the product operator. Also, if $y_i = 0$ for some index and $q < 0$, then we set $M_q(Y) = 0$ since it holds true in the limiting case $y_i \rightarrow 0$. Note that power means have a monotonicity property:

$$M_p(Y) \leq M_q(Y) \text{ for } p \leq q.$$

In practice, we consider $X = R^n$ and A a closed subset of X . For piecewise continuous functions $f: A \rightarrow R^+$, the sum in the power means can be replaced by a (Riemann) integral:

$$M_q(A) = \left(\frac{1}{|A|} \int_A (f(a))^q da \right)^{1/q},$$

with $|A|$ being the volume (or area) of A . The generalized distance transform is thus defined as

$$D_q(x, A) := \left(\frac{1}{|A|} \int_A (d(x, a))^q da \right)^{1/q} \text{ for } q < 0. \quad (3)$$

We obtain the classic distance transform when $q = -\infty$. Note we could also have used the more general Lebesgue integration for the definition of the generalized distance transform, but for the sake of clarity the Riemann integration is more amenable. Specific details on the implementation of an efficient generalized distance transform on binary images are shown in the Appendix.

We can interpret the parameter q as a control on the influence of the contribution of each element of A to the final distance. For $q = -\infty$, only the closest point is considered, whereas for $q = \infty$, only the farthest point is considered. The influence of farther and closer points gradually changes for q in between $-\infty$ and ∞ . When q is small in magnitude, the

influence of each point is roughly equal and we thus expect a distance more robust to outliers. Notice that the smoothness of the distance transform increases as q approaches 0.

We are now ready to state some properties of the GDT.

Proposition 1 (Monotonicity property):

$$D_p(x, A) \leq D_q(x, A) \text{ for } p \leq q. \quad (4)$$

In particular,

$$D(x, A) < D_q(x, A) \text{ for } q > -\infty. \quad (5)$$

Proposition 2 (Vanishing property):

$$D_q(x, A) = 0 \iff x \in A. \quad (6)$$

B. Metrics on Sets

Given the classic Euclidean distance transform D , the Hausdorff distance between sets A and B is defined by

$$H(A, B) := \max(\sup_{x \in A} D(x, B), \sup_{x \in B} D(x, A)), \quad (7)$$

where \sup is the supremum (it can be replaced by the maximum if A and B are closed). The lack of robustness of the Hausdorff metric is well-known. A single outlier can completely throw off the value of the distance. Dubuisson and Jain [17] attempted to make the Hausdorff distance more robust by replacing the supremum and the maximum with an average or with an order statistic. Although a slight gain in robustness was observed experimentally, these modifications destroy the metric properties of the distance.

An equivalent way to express the Hausdorff distance is via the following formula:

$$H(A, B) = \sup_{x \in X} |D(x, A) - D(x, B)|. \quad (8)$$

Baddeley [19] proposed to replace the supremum with a L^p norm. Let w be a concave ($w(x+y) \leq w(x) + w(y)$) and strictly increasing function at 0 ($w(x) = 0$ if and only if $x = 0$), then Baddeley's Delta-metric is defined as

$$\Delta_{p,q}^p(A, B) := \int_X |w(D_q(x, A)) - w(D_q(x, B))|^p dx. \quad (9)$$

This is still a metric and is slightly more robust than the Hausdorff distance.

We generalize the Hausdorff distance and Baddeley's Delta-metric by replacing the classical distance transform with the generalized distance transform:

$$\Delta_{p,q}^p(A, B) := \int_X |w(D_q(x, A)) - w(D_q(x, B))|^p dx. \quad (10)$$

Theorem 1: $\Delta_{p,q}^p$ is a metric.

Proof. To show that $d := \Delta_{p,q}^p$ is also a metric, we need to show the following three properties:

- 1) Identity of indiscernible: $d(A, B) = 0 \iff A = B$.
- 2) Symmetry: $d(A, B) = d(B, A)$.
- 3) Triangular inequality: $d(A, B) + d(B, C) \geq d(A, C)$.

Let $f(x) := w(D_q(x, A))$ and $g(x) := w(D_q(x, B))$. Note that $\Delta_{p,q}^p(A, B) = \|f - g\|_p$. It is well known that the L^p -norm $\|f - g\|_p$ induces a metric on L^p -integrable functions.

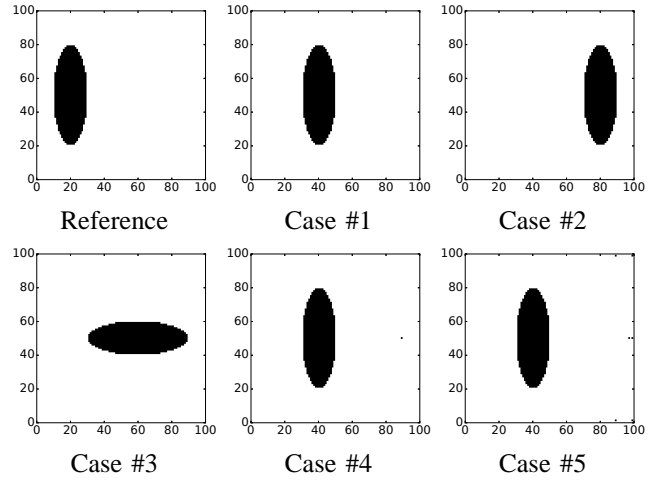


Fig. 2. Toy example with ellipses. Upper-left corner: Reference ellipse centered at (20, 50) with height of 60 units and width of 20 units. Case #1: Same as reference ellipse, but translated 20 units to the right. Case #2: Same as reference ellipse, but translated 60 units to the right. Case #3: Ellipse centered at (60, 50) with height of 20 units and width of 60 units. Case #4: Same as case #1, but with the addition of a disk of radius 1 and centered at (89, 50). Case #5: Same as case #1, but with the addition of 6 disks of radius 1 centered, respectively, at (89, 1), (99, 1), (97, 50), (99, 50), (89, 99) and (99, 99).

The symmetry and the triangular inequality thus follows automatically. It remains to prove the identity of indiscernible.

If $d(A, B) = 0$, then $\|f - g\|_p = 0$, hence we have $f = g$ and $w(D_q(x, A)) = w(D_q(x, B))$. If $x \in A$, then $D_q(x, A) = 0$ by the vanishing property (6). Since $w(x)$ is strictly increasing at 0, we also have $w(D_q(x, A)) = 0$. Since $f = g$, it implies that $w(D_q(x, B)) = 0$ as well. Once again, because $w(x)$ is strictly increasing at 0, we also have $D_q(x, B) = 0$. By the vanishing property (6), it implies $x \in B$. Similarly, if $x \in B$, then $x \in A$. We thus have $A = B$.

On the other hand, if $A = B$, then $f = g$ and $\|f - g\|_p = 0$, thus $d(A, B) = 0$. This completes the proof.

We illustrate the difference between the Hausdorff distance, Baddeley's Delta-metric and our proposed generalization by computing the distances between a reference ellipse and ellipses for five different cases given in Fig. 2. This example is inspired by a similar experiment found in [20]. For comparison, we also include Jaccard's distance:

$$J(A, B) = 1 - \frac{|A \cap B|}{|A \cup B|}. \quad (11)$$

Jaccard's distance is a transformation of Jaccard's index, also known in meteorology as the Threat Score (TS) or the Critical Success Index (CSI). Any other score based on a contingency table will behave in a similar fashion.

Scores are summarized in Table I. We observe that Jaccard's distance is 0 for all cases. This is easily explained by the fact that none of ellipses in the five cases intersect with the reference ellipse. That is, Jaccard's distance and other contingency-based scores cannot differentiate between a miss and a near miss. The Hausdorff distance for Cases #2 and #3 is exactly the same as the magnitude of the translation of the ellipses, which is a nice feature for this distance. However,

TABLE I
COMPARISON OF JACCARD'S, HAUSSORFF'S AND BADDELEY'S
DISTANCES WITH THE PROPOSED DISTANCE FOR THE 5 CASES FROM
FIG. 2.

| Case | Jaccard | Hausdorff | Baddeley | Proposed |
|------|---------|-----------|----------|----------|
| 1 | 1.0 | 20.0 | 16.5 | 18.5 |
| 2 | 1.0 | 60.0 | 42.4 | 44.2 |
| 3 | 1.0 | 60.0 | 27.7 | 30.7 |
| 4 | 1.0 | 60.0 | 23.0 | 18.7 |
| 5 | 1.0 | 77.3 | 27.8 | 19.7 |

only the farthest pixel influences the distance, this is why the scores are the same for Cases #2, #3 and #4 even though Case #4 is more similar to Case #1 with only a single outlier. Baddeley's Delta-metric does better, with reasonable scores for Cases #1-#4, although one could argue that it is slightly over-sensitive for Case #4. However, when more outliers are added as in Case #5, then Baddeley's Delta-metric fails as the distance for Case #5 is slightly greater than the one for Case #3 despite Case #5 being more similar to the reference ellipse. The proposed generalization of Baddeley's Delta-metric and the Hausdorff distance gives the most intuitive result. The distance is the smallest for Case #1 and increases only slightly for Cases #4 and #5. Case #3 is second to last in the ranking and Case #2 is the worst of the five.

III. SMOOTHNESS

A. Curvature of Level-sets

We want to analyze the smoothness of the level sets of the generalized distance transform as a function of the parameter q . We consider the case $A_1 = \{(-1, 0), (1, 0)\}$ in R^2 with the counting measure as a minimal example and as a prototype for more general examples. For this case, the generalized distance transform of A_1 is

$$\phi(x, y) = \left(\frac{((x+1)^2 + y^2)^{q/2}}{2} + \frac{((x-1)^2 + y^2)^{q/2}}{2} \right)^{1/q}.$$

The smoothness of the generalized distance transform for different q can be compared in Fig. 3. Note that in the case $q = -\infty$, i.e. for the classic Euclidean distance transform, sharp ridges are present along $\{(x, y) \in R^2 | x = 0\}$, which is the line at equal distance between the two points of A_1 .

These qualitative results can be expressed quantitatively by computing the curvature of the level set curves. The curvature of a curve defined implicitly from the level set function ϕ is given by

$$\kappa = \nabla \cdot \frac{\nabla \phi}{|\nabla \phi|}. \quad (12)$$

Developing for the two-dimensional case $\phi : R^2 \rightarrow R$, we obtain

$$\kappa = \frac{\phi_{xx} + \phi_{yy} - 1}{(\phi_x^2 + \phi_y^2)^{3/2}}, \quad (13)$$

where ϕ_x and ϕ_y are the partial derivatives of ϕ with respect to, respectively, the first and the second component, and ϕ_{xx} and ϕ_{yy} are second-order partial derivatives.

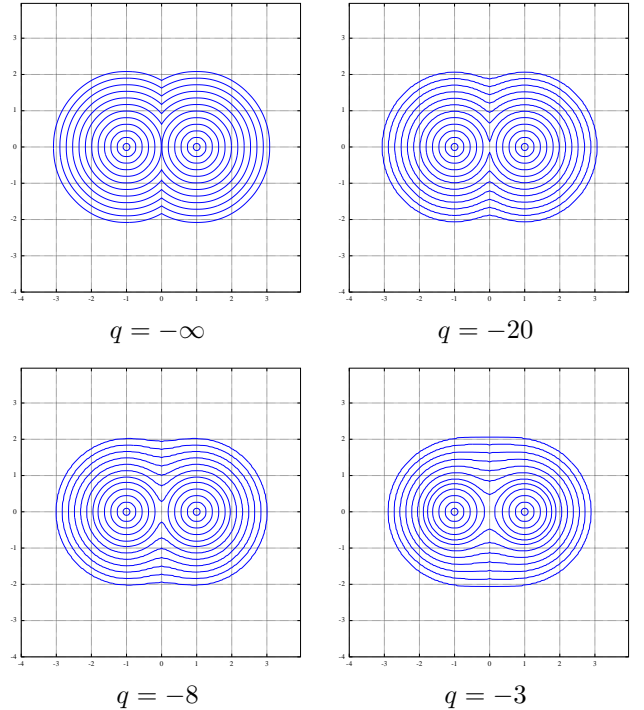


Fig. 3. Smoothness of the (rescaled) generalized distance transform for different values of q . Note the increasing smoothness for q closer to 0.

For our example, we have

$$\kappa(0, y) = \frac{1}{|y|} \left(\frac{y^2 + q}{y^2 + 1} - (y^2 + 1)^{1/2} \right).$$

From this expression, it follows that along the line of equal distance, the curvature is always negative, with a sharper curvature for q decreasing towards $-\infty$. Notice that for any q , there is a cusp at $(x, y) = (0, 0)$. This can be explained by the fact that this point is the location where the level-sets merge. So even though the contours can be made generally smoother with increasing q , there are situations for which sharpness is inevitable. For example, when the boundary of the set A itself is sharp, the level-sets around the boundary will have similar sharpness.

B. Contour Evolution

The generalized distance transform can be used to smoothly modify the shape of a set A . We can compare this proposed method with two other traditional methods.

In mathematical morphology [1], [21], a set is modified (dilated or eroded) by a structuring element. If the structuring element is a ball (or disk) of radius r , then morphological dilation is equivalent to finding the contours of the Euclidean distance transform at level r .

In numerical analysis, an interface between two media –a front– can be propagated according to the Eikonal equation

$$|\nabla \phi(x, y)| = F(x, y)$$

subject to $\phi(x, y) = 0$ on ∂A with $F(x, y) > 0$. The Fast Marching Method (FMM) solves this equation efficiently [2].

For the particular case $F(x, y) = 1$, the solution of the Eikonal equation is the signed distance transform. A front can also evolve according to some other PDEs following level set methods.

A contour evolution algorithm based on the GDT simply combines the generalized distance transform with a contouring algorithm. Given an initial set A of points, the signed generalized distance transform $\phi(x)$ is then computed. Finally, contours can be extracted with $C(t) = \{x : \phi(x) = v(t)\}$ with $v(t) > 0$ for expanding contours and $v(t) < 0$ for contracting contours.

In Figure 4, we compare different methods and parameters for contour evolution starting from the triple sine example of Sethian [2]. The contour evolution solves the equation

$$\frac{\partial \phi(x, t)}{\partial t} = (1 - b\kappa)|\nabla \phi(x, t)|, \quad (14)$$

where κ is the local curvature given in (12) and b is the speed parameter. The LSM does not guarantee that the contour is moving forward and in fact we can see that it crosses itself for the cases $b = 0.05$ and $b = 0.1$. Only the case $b = 0$ ensures a forward motion of the contours, but since this case is equivalent to the classical distance transform, it also suffers the same smoothness problem. The closer the parameter q is to 0, the smoother the contours are.

IV. ROBUSTNESS

A. Analysis

Let A and B be two bounded sets for which we want to compute their distance. The lack of robustness of the Hausdorff distance to outliers is easily illustrated by adding a single point outside either A or B . Baddeley [19] showed that his proposed distance is more robust to outliers, but we can devise the following simple counter-example to demonstrate a case where it fails.

Let A be a set of unit area and let $B = B_{\mu, \lambda}$ be a perturbed set obtained by adding a set of area μ at a distance λ from A . For simplification, we assume that the perturbation is concentrated into a point called y and the set A is concentrated at a point a . We want to know if the distance is continuous with respect to μ . That is, we want to check if the limit of the distance between A and $B_{\mu, \lambda}$ vanishes when $\mu \rightarrow 0$. The setting is illustrated in Fig. 5.

For the Hausdorff distance, we have $D_A(y) = \lambda$ and $D_B(x) = 0$ for $x \in A$. It implies that $h(A, B) = \lambda$ for all $\mu > 0$.

For Baddeley's Delta-metric, we compute

$$\Delta_p^p(A, B) = \left(\frac{1}{|W|} \int |D(w, B) - D(w, A)|^p dw \right)^{1/p},$$

with

$$|D(w, B) - D(w, A)| = \max(0, \|y - w\| - \|a - w\|).$$

This does not depend on μ , which means that even for a negligibly small area added to A , the distance $\Delta_p(A, B)$ will always stay the same.

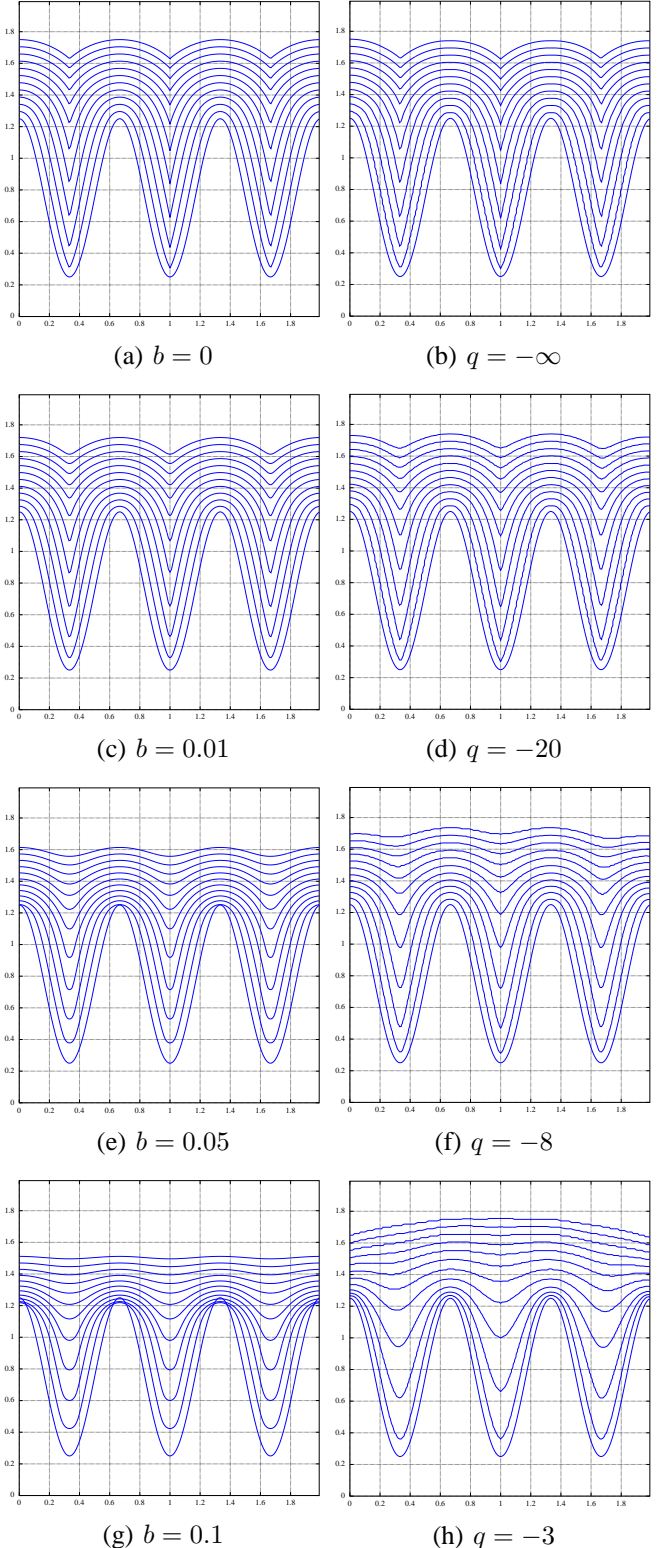


Fig. 4. Contour evolution comparison for LSM and GDT methods. First column: LSM [22] with parameter b from (14). Second column: GDT with parameter q from (3). Both methods can control the smoothness of the contours with their parameters. However, notice the self-intersection of contours when b is larger. On the other hand, the GDT guarantees monotonicity of the contours. The case $q = -\infty$ is equivalent to $b = 0$. A rescaling of the GDT was used to adjust the speed of the contour evolution.

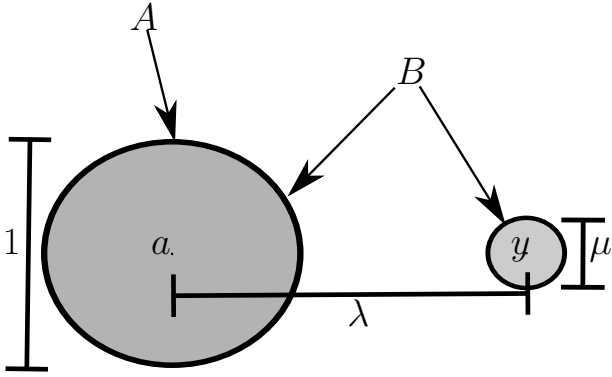


Fig. 5. Illustration of the counter-example. The set A is concentrated around the point a and weights a unit mass. The set B is the union of the set A and of an other set concentrated around the point y and with a mass μ . The distance between a and y is λ . Keeping the distance λ constant, the mass μ is reduced to an infinitesimal value.

On the other hand, for the proposed metric

$$\Delta_{p,q}(A, B) = \left(\frac{1}{|W|} \int |D_q(w, B) - D_q(w, A)|^p dw \right)^{1/p},$$

the distance vanishes as $\mu \rightarrow 0$ since

$$D_q(w, B) = \frac{(\|a - w\|^q + \mu\|y - w\|^q)^{1/q}}{1 + \mu}$$

and

$$D_q(w, A) = \|a - w\|.$$

B. Synthetic Experiments

We want to empirically verify the theoretical result related to the robustness of the generalized Hausdorff metric. In a first experiment, we compare the distance between an image of a binary disk and corrupted versions of it. Since different distances can have different scales, we normalize them by computing the skill score

$$SS = \frac{d - d_{\text{ref}}}{d_{\text{min}} - d_{\text{ref}}} = 1 - \frac{d}{d_{\text{ref}}}$$

with the distance to a random noise image as the reference distance d_{ref} and the distance between two identical sets as the minimal distance $d_{\text{min}} = 0$. Thus, a 100% skill score corresponds to a distance close to zero between the original image and its corrupted version whereas a skill score close to zero means that the distance between the original and the corrupted version of the disk is of the same order of magnitude than the distance between the original disk and the random noise image. A robust metric will give a gradually decreasing skill for corrupted, but still recognizable images, whereas a non-robust metric will not differentiate between random noise and slightly corrupted images.

We define the original image as a disk of radius of ten units centered in a 200 by 200 pixels grid. A noisy image is generated by randomly setting half the pixels to white and the other half to black. The original and the random image are shown in Fig. 6.



Fig. 6. Left: the original (uncorrupted) disk image. Right: a random image used to compute the reference distance. If the distance between the original image and a corrupted version of it is similar to the distance between the original image and the random image, we can thus conclude that the distance is not robust to that corruption model.

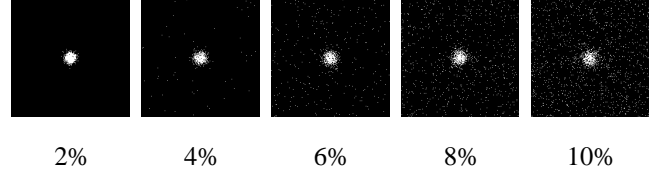


Fig. 7. Image corrupted by white Gaussian noise with different noise levels (relative standard deviation of the Gaussian distribution compared to the dynamic range). At the 2% level, the image corruption is concentrated around the disk, but for higher noise levels the corruption extends farther.

For the purpose of our noise corruption model, we assume that the original image was obtained by thresholding a Gaussian kernel

$$f(x, y) = \exp\left(-\frac{1}{2} \frac{(x - 100)^2 + (y - 100)^2}{10^2}\right)$$

at the level $C = \exp(-1/2)$. In the first corruption model we add white Gaussian noise to the Gaussian kernel with standard deviation (noise level) between 0 and 0.1 and then we threshold back the resulting image at $C = \exp(-1/2)$. Figure 7 illustrates the kind of image corruption obtained with this simulation procedure.

In the second corruption model, we randomly flip the pixels from either black to white or from white to black. We randomly select a permutation order of the image pixels and gradually flip up to 25% of the pixels of the original image. Figure 8 shows the some images obtained by this corruption model.

We then computed the distance between the original image and the corrupted images and derived the skill scores for the Hausdorff distance, the Baddeley distance and the proposed generalized Hausdorff distance. We repeated the experiment 20 times in order to take into account the variability of the distance in function of the sample drawn. Results are shown in Fig. 9.

For the Gaussian noise corruption model, this variability is the greatest between 2% and 4%. This can be explained by

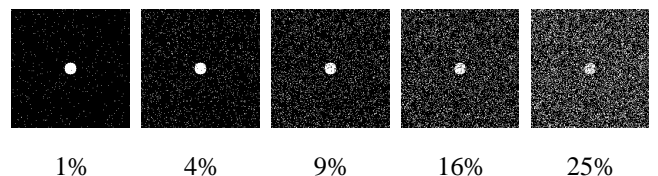


Fig. 8. Image corrupted by salt-and-pepper noise with different noise levels (percentage of flipped pixels). The corruption is non-local for any noise level.

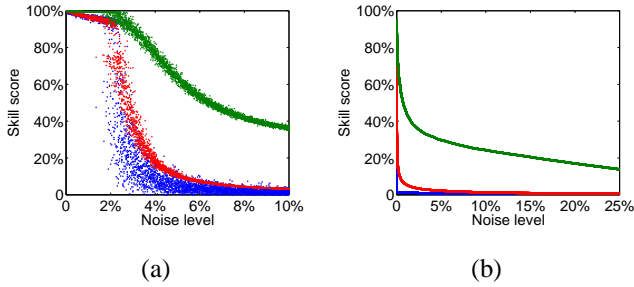


Fig. 9. Comparison of the robustness to noise for the Hausdorff distance (blue), the Baddeley distance (red) and the proposed distance (green). (a) White Gaussian noise. (b) Salt-and-pepper noise. For the Gaussian noise, the three distances are robust up to 2% levels, but then both the Hausdorff distance and the Baddeley distance exhibit a sharp decrease of skill even though the corrupted images are still recognizable. On the other hand, the proposed distance shows a more graceful degradation in skill as the noise level increases. For the salt-and-pepper noise, the Hausdorff distance loses all skill even for a single switched pixel. Baddeley’s Delta-metric does not do much better. Only the proposed distance retains skill at all levels of noise.

the fact that at this noise level, the corrupted image may or may not have outliers far away from the disk. For the salt-and-pepper noise model, the way the experiment is done guarantees an increasing distance and a decreasing skill score as the noise level increases. The Baddeley distance and the proposed generalized Hausdorff distance are consistent for all samples, whereas the Hausdorff distance shows more variation but has generally a lower skill score than the Baddeley distance. For clarity, we only showed the skill score for the first sequence of samples.

In a second experiment, we computed the distance between the original disk image and a translated image in the presence of salt-and-pepper noise, as shown in Fig. 10. For a horizontal translation of up to 50 units, we computed the Hausdorff distance, Baddeley distance and the proposed distance for four levels of noise: no noise, 0.01%, 0.1% and 1%. Results are compared in Fig. 11. The Hausdorff distance computes the exact magnitude of a translation in the absence of noise, whereas both Baddeley’s Delta-metric and the proposed generalization underestimate the magnitude of the translation by the same factor. However, for the lowest level of noise, the proposed distance is insensitive to noise, whereas the Baddeley distance can slightly differentiate between small and large translations. The Hausdorff distance is totally incapable of differentiating between different translations even with the presence of the slightest noise.

V. APPLICATIONS

Here we present real-world applications of the techniques developed in this paper related to weather analysis and forecasting, this being the specific application in which we are interested. However, we expect that the techniques presented are general enough that several other applications in computer vision and image processing are possible, and in particular applications using remotely sensed data.

A. Object-based Weather Forecasting and Analysis

Weather forecasting is a complex process with multiple layers [23]. Observations are collected periodically with point

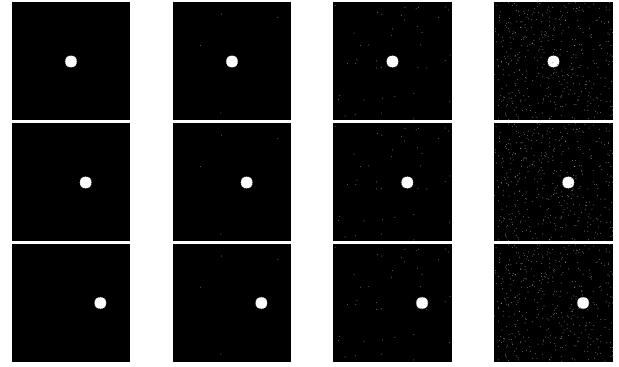


Fig. 10. Disk images translated and corrupted by salt-and-pepper noise. First row: no translation. Second row: translation of 25 units. Third row: translation of 50 units. First column: no noise. Second column: 0.01% noise. Third column: 0.1% noise. Fourth column: 1% noise.

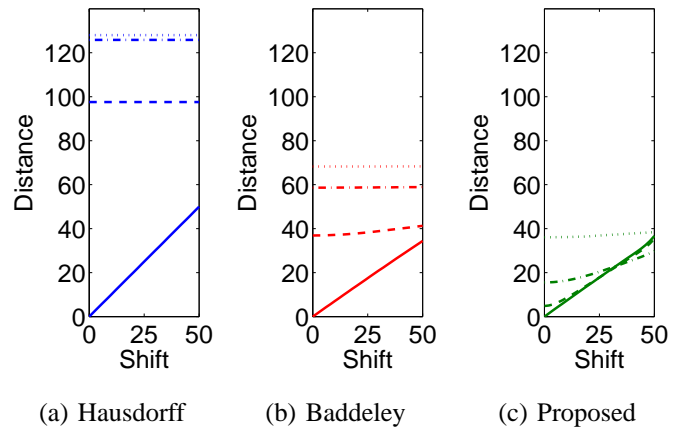


Fig. 11. Comparison of the robustness to noise for (a) the Hausdorff distance (blue), (b) the Baddeley distance (red) and (c) the proposed distance (green). For each distance measure, four levels of salt-and-pepper noise were compared: no noise (full line), 0.01% noise (dashed line), 0.1% noise (dash-dotted line) and 1% noise (dotted line). The Hausdorff distance could not differentiate between the original and the translated images in the presence of noise. Baddeley’s Delta-metric only weakly differentiated between images. Only the proposed distance robustly estimated the translation magnitude in the presence of noise.

sensors or by remote sensing. These observations are assimilated together to obtain an estimate of the current state of the atmosphere. This serves as the initial conditions for a numerical model describing the known physics of the atmosphere as a system of partial differential equations, called Numerical Weather Prediction (NWP). This system is solved by a computer that generates periodic output for a specified number of days (called model ‘guidance’).

Traditionally, forecasts and warnings are provided for a few key locations at specified ‘issue’ times. Increasingly, there is a desire to move away from this forecasting method to an on-demand forecast for any location at any time. Although NWP model guidance exhibits this spatial and temporal resolution, it often needs to be modified by the forecaster based on other information (e.g., recent observations, known model biases, conceptual models, guidance from other NWP models). Given the high dimensionality of the data, it is necessary to reduce resolution in order to facilitate forecaster modifications in both space and time.

The object-based approach [24] is a paradigm that allows an intuitive simplification by representing important meteorological features as lines, areas and tracks (called MetObjects).

MetObjects automatically derived from NWP model guidance or observational analyses can serve as a 'first guess' that forecasters modify if/when necessary. Object-based verification approaches [25] are also desired. Both are discussed in the following sections.

B. First-Guess MetObjects

It is anticipated that the generation and use of first-guess MetObjects (FGMOs) will reduce the workload of the forecaster. While 'best data' FGMOs would capture the essence of the NWP model guidance at a relatively high resolution, 'best form' FGMOs will further simplify the NWP model guidance to allow for forecaster modification when necessary, comprising a smaller set of lower-resolution objects that are much easier to manipulate.

In addition, we want a simplified vector representation that will allow an interface with a Geographic Information System (GIS) and enable automated delivery of the weather forecast.

For this paper, we generate an example of FGMOs from lightning observations obtained from the Southern Ontario Lightning Mapping Array (SOLMA) [26]. We compare these MetObjects with FGMOs derived from a lightning diagnostic implemented in an experimental version of the Canadian High-Resolution Deterministic Prediction System (HRDPS) [27].

Lightning Mapping Arrays (LMAs) [28] are networks of ground stations that detect very high-frequency (VHF) signals generated by lightning sources. Using the Global Positioning System (GPS) and time-of-arrival techniques, lightning sources are located in three spatial dimensions at high time resolution. It is thus a ground-based remote sensing application. The SOLMA has 14 such stations in its network.

The Canadian HRDPS numerical model with the lightning diagnostic of McCaul et al. [29] was run experimentally over southern Ontario during Summer 2015. It consists of three cascading grids having horizontal grid spacing of 2.5 km, 1 km and 250 m.

We study the August 2nd, 2015 case, a day of severe weather in southern Ontario with two successive lines of storms that generated a total of four tornadoes.

For the SOLMA, we mapped sources that were detected by at least 8 ground antennas over a period of one hour (between 22 and 23 UTC) and computed the source density on the HRDPS 1024×1024 grid. Typically, tens to thousands of sources represent a single lightning flash. We then estimated the lightning flash extent by considering all grid cells with at least one source. The authors noticed that over the period of interest the HRDPS tended to generate considerably more deep, moist convection than observed. For this reason, only grid cells having at least eight (8) model lightning flashes over the same 1-hour period were considered. Original and thresholded data are shown in Fig. 12(a-d).

Using the distance transform, we then applied a dilation of 40 pixels radius (10km) to both the SOLMA and HRDPS thresholded data. We also dilated the data using the GDT with

$q = -2$, a radius of influence of $r = 100$ grid cells and a threshold of $c = 1000$. Results can be compared in Fig. 12(e-h).

The generation of FGMOs makes interpretation of the lightning forecasts and observations straightforward. The HRDPS forecast predicts thunderstorm activity mainly in one diagonal with more activity on the left side and on the top right corner of the map. It also predicts some more lightning activity on the right hand side and weak lightning activity towards the top left corner. On the other hand, the observed lightning tells a much simpler story. The main storm activity was concentrated along Lake Ontario (middle right side of the image), with some scattered thunderstorms on the top-left of the map. Both types of dilation allows a similar interpretation of the forecast and of the observations.

However, the dilation using the classical distance transform introduces 'cartoon cloud' artifacts, whereas the GDT-based dilation is smoother. Notice also the small 'speckles' generated by the GDT-based dilation on lower left part of Fig. 12(h). They are due to the presence of noise in the LMA data. Because of the robustness of the GDT, they are not overly dilated as it is the case for the classical DT Fig. 12(f). A post-processing step could be applied to remove these small areas so the human forecaster does not have to manipulate them.

C. Forecast Verification

Forecast verification aims to assess the quality of a weather forecast by comparing the forecast with either observations or numerical model analyses. Verification scores can then be computed to quantify the closeness between observations and forecast. Traditional verification scores, such as critical success index (CSI), probability of detection (POD) and probability of false detection (POFD) do a point-by-point comparison using contingency tables (see [30], chapter 7). For high-resolution numerical models, it has been observed that these scores do not convey well the quality of forecast due to the 'double penalty' problem (see e.g. [31]). Several alternatives have been proposed in the literature [25], with Hausdorff distance and Baddeley's Delta-metric [32] categorized as two kinds of location measures.

We want to compare scores from the Hausdorff distance, Baddeley's Delta-metric and our proposed metric with subjective (forecaster) rankings for a certain forecast. This is a meta-verification problem. A full subjective experiment would involve collecting the Mean Opinion Score of several forecasters for several cases and goes beyond the scope of this article.

As an example, consider a case of cloud coverage verification on May 26th, 2015 over French Guiana and other parts of South America. This dataset is part of the Cayenne campaign for the high ice water content research project [33]. The Canadian numerical weather model [34] was initialized at 0:00 UTC and run over a limited area using 10-km horizontal grid spacing. The true cloud coverage weather element [35] was then extracted. We also took the GOES-13 cloud coverage product [36] and cropped it so that all grid points fall within the limited area model domain. We then reprojected the model

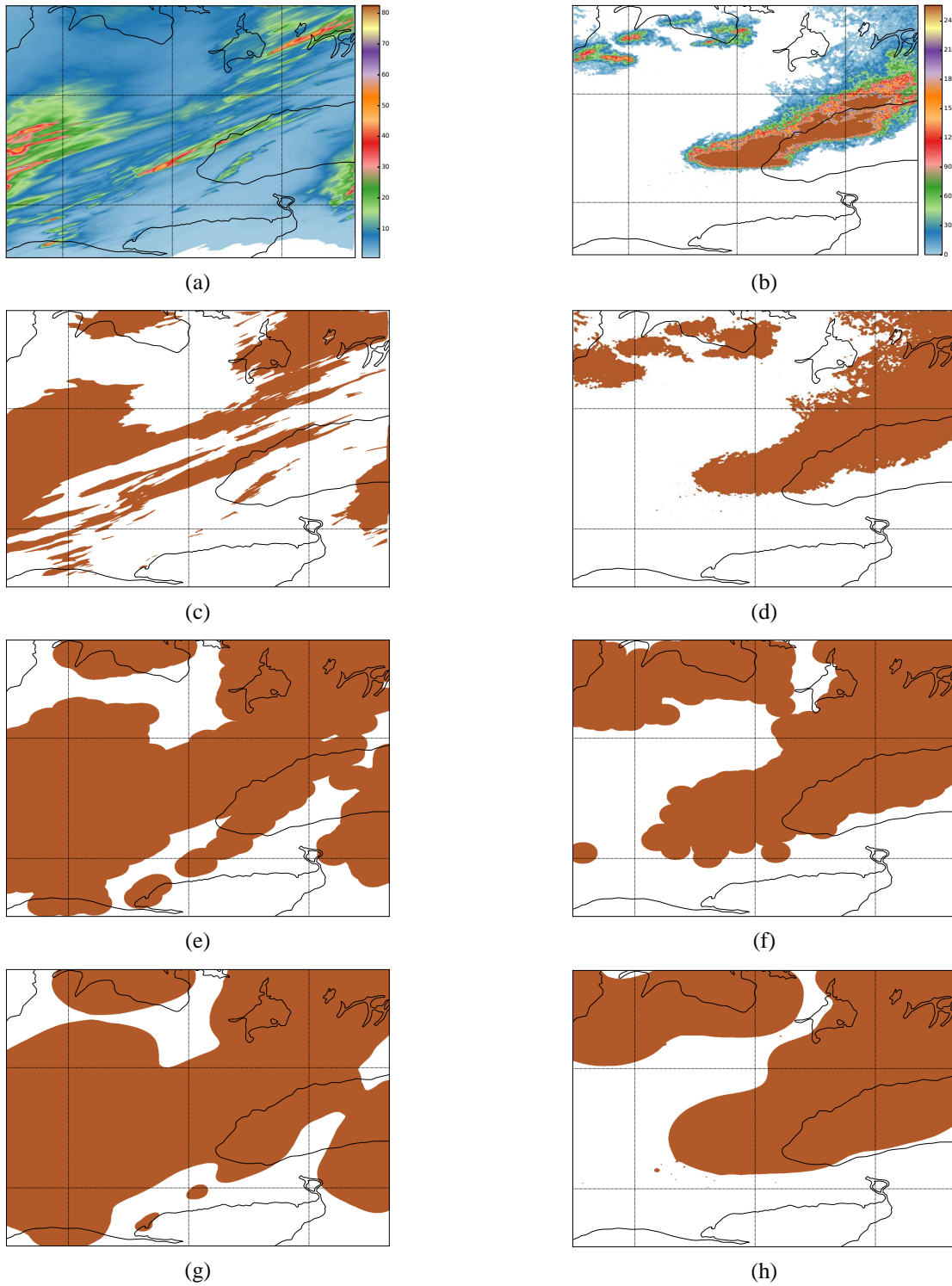


Fig. 12. Generation of First-guess areas for thunderstorm MetObjects. (a) Original thunderstorm forecast. (b) Original lightning observations. (c) Thresholded forecast at 8 flashes per grid cell. (d) Thresholded lightning data at 1 source per grid cell. (e) Dilation of the thresholded forecast data according to the distance transform. (f) Dilation of the thresholded lightning data according to the distance transform. (g) Dilation of the thresholded forecast data according to the GDT. (h) Dilation of the thresholded lightning data according to the GDT.

data to the satellite imagery grid using bilinear interpolation and applied a threshold at 10% for the true cloud coverage weather element to obtain a binary image. We consider the model outputs between 9:15 and 20:45 UTC and compare them with the satellite cloud coverage product as well as with a persistence forecast consisting of the 9:15 UTC satellite observation.

For each time step of 30 minutes, we computed the Hausdorff distance, Baddeley’s Delta-metric (with $p = 2$) and our proposed metric between model prediction and satellite observation as well as between the persistence forecast and the current satellite observation (see Fig. 13).

The parameters we used for the computation of our proposed metric were $p = 2$, $q = -2$, $r = 100$ and $c = 1000$ (see (10) and Appendix for details). This choice is arbitrary, but we found it is convenient for computation. Also, by taking a value of q close to 0, we put less weights on the outliers.

As the three scores have the properties of a metric, they are all zero at 9:15 when comparing the persistence forecast against itself. The three metrics differ on when they indicate that the model prediction is better than the persistence forecast. According to Hausdorff distance, the persistence forecast is better only for the first hour, then the persistence forecast and the model forecast cross-over several times between 10:15 and 16:15, and the model forecast ends up with a lower Hausdorff distance afterwards. For Baddeley’s Delta-metric the first cross-over occurs around 16:45, then the model prediction has lower distance until 19:45, and finally the persistence forecast and the model forecast have similar Baddeley’s Delta-metric between 19:45 and 20:45. For the proposed distance the persistence forecast has consistently a smaller distance for the 12 hours studied. In Fig. 14, we compare visually the persistence forecast with the numerical prediction at four different times. Four all the cases, the persistence forecast at 9:15 UTC looks subjectively better than the model output from the 0:00 UTC run. It thus means that of the three verification measure, the proposed metric is the one that better correlates with subjective judgement for that particular example.

Note that the proposed distance is smoother as a function of lead time, whereas Hausdorff and Baddeley distances have greater variability. Smoothness is a desired property insofar it is intuitively expected that the forecast quality will gradually degrade as a function of the lead time, something that is generally observed when estimating the predictability of a forecast method [37]. However, smoothness is not a necessary condition for a good distance measure since the smoothness also depends on the forecasting method and on the variability of the predictability of the observed phenomenon. Nevertheless, we hypothesize that the lack of smoothness of the Hausdorff and Baddeley distances might be caused by their lack of robustness to outliers.

The distance metric derived from the Generalized Distance Transform could also be used for comparing the similarity between MetObjects, particularly those defined by contours. Since the distance transform is mathematically defined for sets, this could in theory include the comparison of lines and clouds of points as well. Moreover, certain object-based techniques such as MODE [38] sometimes use the geometric

distance between matched objects as one of the features to be compared.

VI. CONCLUSION

We introduced a modification of the classical distance transform that is smoother and that leads to a more robust distance between binary images.

The proposed Generalized Distance Transform and its associated generalized Hausdorff metric are prime candidates to replace their classical counterparts in numerous applications. We focused on two simple ones: the dilation of sets for weather analysis and forecasting, and the computation of spatial distance between dichotomous forecasts and observations.

As the proposed techniques are general, they are also readily applicable for processing aerial remote sensing data. For example, we can use the GDT to obtain an envelope of cloud cover as measured by satellite imagery. Also, we can compute a generalized distance between forecasts and satellite observations for weather-related products such as cloud cover and cloud-top temperature for the purpose of verification. Two other possible applications in geophysics could be the analysis of high-resolution topography data from LiDAR [39] and comparing or processing curves of meandering rivers from satellite images. In both these applications the smoothness of the transform and its dependence to the local curvature of the curves are desirable properties.

A trade-off that needs to be taken into account is the computational speed of the proposed GDT. Empirical experiments indicate that the computational speed is about one order of magnitude slower for the GDT compared to the classical distance transform, but this of course depends on the specific implementation of the algorithms.

The potential applications were only briefly explored. For first guesses, other smoothing methods could also be considered, possibly in combination, and a full calibration and validation experiment is planned as future work. For the object-based verification, a subjective experiment is also planned so that the proposed metric can be correlated with subjective scores. Finally, combining the FGMO techniques with the generalized Hausdorff distance could lead to a new kind of MetObject-based verification method.

APPENDIX A COMPUTATIONAL METHODS

A. Local Estimate

The computation of the GDT involves a summation over all the points of the set A for each point in X . A direct implementation could then take up to $O(N^2)$ operations for a grid of $N = N_x N_y$ pixels. In general, we are only interested in the points of X that are close to the boundary of A . Indeed, for Baddeley’s Delta-Metric a constant c can be set up as the maximum distance transform.

A more efficient estimate only takes the points in X than are less than a radius r from A . That is to say that the value of each point is only affected locally within a radius of influence. This way, we can implement the GDT as a convolution. Indeed, let

$$I_A(x) = \begin{cases} 1 & \text{if } x \in A, \\ 0 & \text{otherwise,} \end{cases}$$

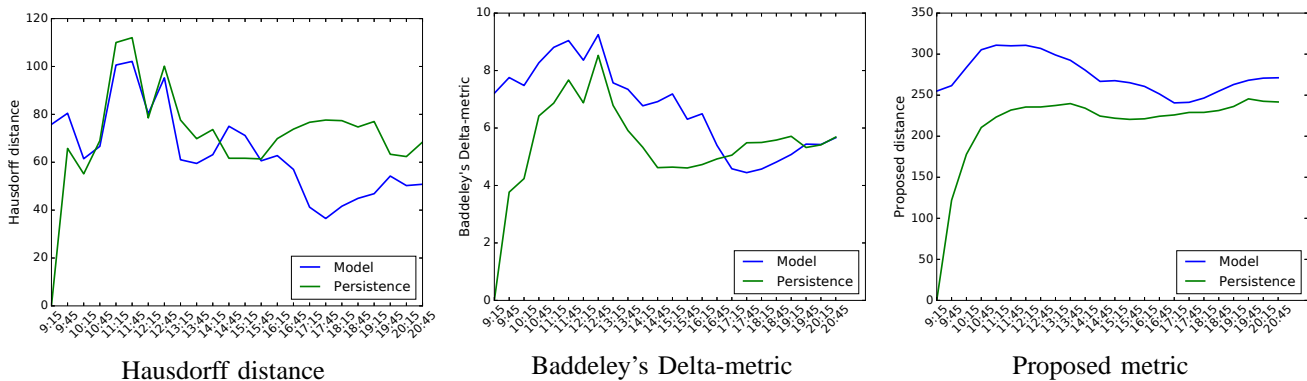


Fig. 13. Comparison of the distance between numerical prediction and satellite observation versus the distance between a persistence forecast and the same satellite observation according to three different verification measures: Hausdorff distance, Baddeley's Delta-metric and our proposed metric based on the Generalized Distance Transform.

be the characteristic function of A . We define the following convolution kernel:

$$g(x) = \begin{cases} \|x\|^q & \text{if } 0 < \|x\| \leq r, \\ 0 & \text{otherwise.} \end{cases} \quad (15)$$

The centre of the kernel is set to zero to avoid any division by zero when $x \in A$. We then have

$$\begin{aligned} D_q(x, A) &= \left(\frac{1}{|A|} \int_A d^q(x, a) da \right)^{1/q} \\ &= \left(\frac{1}{|A|} \int_X I_A(y) d^q(x, y) dy \right)^{1/q} \\ &= \left(\frac{1}{|A|} (I_A * g)(x) \right)^{1/q}. \end{aligned} \quad (16)$$

We then compute $w(D_q(x, A), c)$ with

$$w(y, c) = \begin{cases} y & \text{if } y < c, \\ c & \text{otherwise.} \end{cases}$$

These computations are valid for all x such that $0 < D(x, A) \leq r$. Otherwise, we will have $(I_A * g)(x) = 0$ and $D_q(x, A)$ will grow to infinity when taking the negative exponent. We thus handle the special cases $D(x, A) = 0$ and $D(x, A) > r$ separately. If $D(x, A) = 0$, then $x \in A$ and we can directly set $D_q(x, A) = 0$. If $D(x, A) > r$, then by the monotonicity property (5), the GDT is also greater than r . It means that truncating the convolution kernel at $\|x\| = r$ will not affect the computation of $w(D_q(x, A), c)$ only if $c \leq r$. In practice, we could have $c > r$, so an approximation of $w(D_q(x, A), c)$ needs to be done. We thus set $w(D_q(x, A), c) = c$ whenever $D(x, A) > r$.

To summarize, the steps for the computation of the GDT are as follows:

- 1) By default, set $r = 50, c = 100$ and $q = -2$.
- 2) Compute the convolution filter g following (15).
- 3) Compute the distance transform $D_q(x, A)$ with (16).
- 4) Compute $w(D_q(x, A), c)$, separating in three cases:

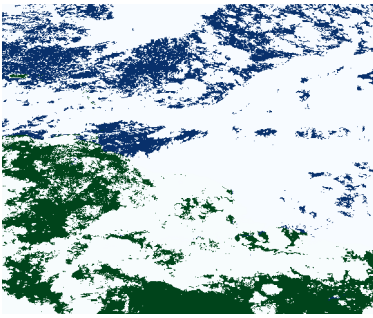
$$w(D_q(x, A), c) = \begin{cases} 0 & \text{if } D(x, A) = 0, \\ \min(D_q(x, A), c) & \text{if } 0 < D(x, A) \leq r, \\ c & \text{if } D(x, A) > r. \end{cases}$$

ACKNOWLEDGMENT

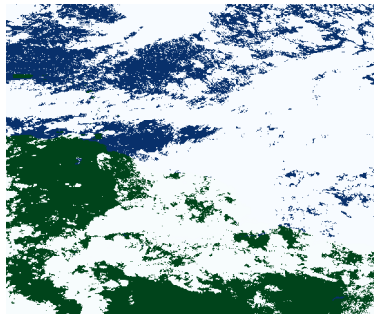
The authors would like to thank Norbert Driedger and Barbara Casati for reviewing an earlier version of the manuscript and for useful discussions. We would also like to thank Jason Milbrandt and Anna Glazer for providing the HRDPS data, Helen Yang for the help with preprocessing the LMA data and Zhipeng Qu for providing the satellite imagery and model data for the cloud coverage example. Finally we would like to extend some special thanks to Emma Hung for technical support with data processing.

REFERENCES

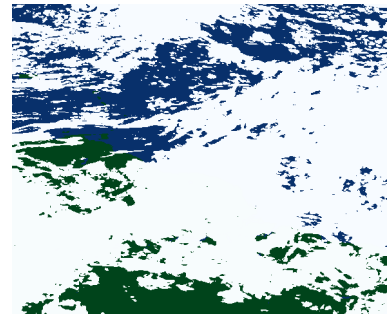
- [1] F. Y. Shih, *Image processing and mathematical morphology: fundamentals and applications*. Boca Raton: CRC Press, 2009.
- [2] J. A. Sethian, *Level Set Methods and Fast Marching Methods*, 2nd ed. Cambridge University Press, 1999.
- [3] D. W. Paglieroni, "Distance transforms: Properties and machine vision applications," *CVGIP: Graphical Models and Image Processing*, vol. 54, no. 1, pp. 56 – 74, 1992.
- [4] L. J. Latecki, Q.-n. Li, X. Bai, and W.-y. Liu, "Skeletonization using SSM of the distance transform," in *IEEE Int. Conf. Image Process.*, vol. 5. IEEE, 2007, pp. V-349.
- [5] M. Kowalczyk, P. Koza, P. Kupidura, and J. Marciniak, "Application of mathematical morphology operations for simplification and improvement of correlation of images in close-range photogrammetry," *The Int. Arch. Photogram. Rem. Sens. Spatial Inform. Sci.*, vol. 37, no. Part B5, 2008.
- [6] S. Osher and R. P. Fedkiw, *Level set methods and dynamic implicit surfaces*, ser. Applied mathematical science. New York, N.Y.: Springer, 2003.
- [7] D. P. Huttenlocher, G. A. Klanderman, and W. J. Rucklidge, "Comparing images using the hausdorff distance," *IEEE Trans. Pattern Anal. Mach. Intell.*, vol. 15, pp. 850–863, 1993.
- [8] N. Paragios, M. Rousson, and V. Ramesh, "Non-rigid registration using distance functions," *Comput. Vis. Image Underst.*, vol. 89, no. 2-3, pp. 142–165, 2003.
- [9] D. Brunet and D. Sills, "An implicit contour morphing framework with applications for computer-aided severe weather forecasting," *IEEE Signal Process. Lett.*, vol. 22, no. 11, pp. 1936–1939, 2015.
- [10] B. S. D. Sagar, *Mathematical Morphology in Geomorphology and GISci*, 1st ed. Chapman & Hall/CRC, 2013.
- [11] P. Soille and M. Pesaresi, "Advances in mathematical morphology applied to geoscience and remote sensing," *IEEE Trans. Geosci. Remote Sens.*, vol. 40, no. 9, pp. 2042–2055, 2002.
- [12] S. Aksoy, C. Tusk, K. Koperski, and G. Marchisio, "Scene modeling and image mining with a visual grammar," in *Frontiers of remote sensing information processing*. World Scientific, 2003, pp. 35–62.



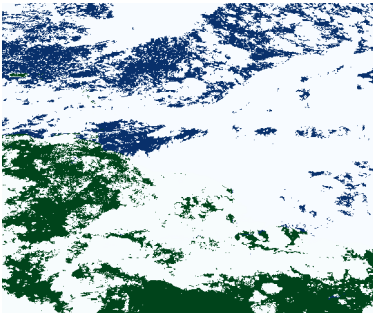
Satellite cloud coverage at 9:15



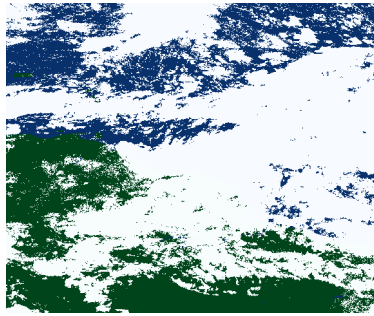
Satellite cloud coverage at 10:45



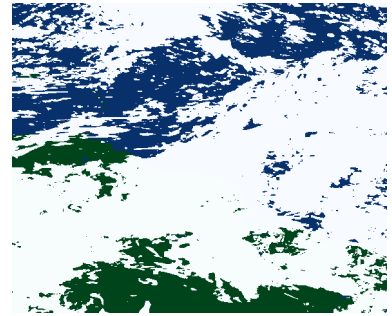
Numerical prediction at 10:45



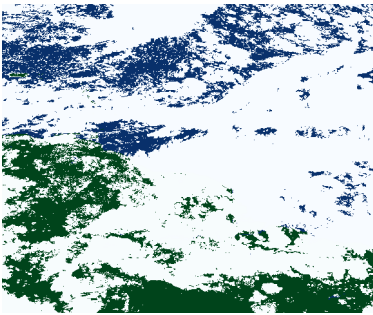
Satellite cloud coverage at 9:15



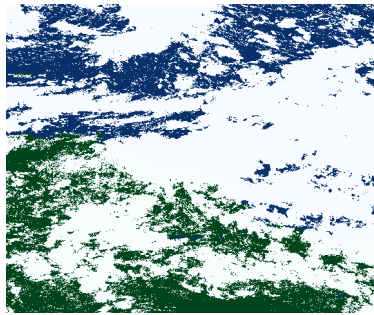
Satellite cloud coverage at 13:45



Numerical prediction at 13:45



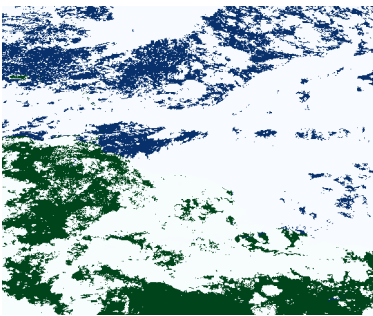
Satellite cloud coverage at 9:15



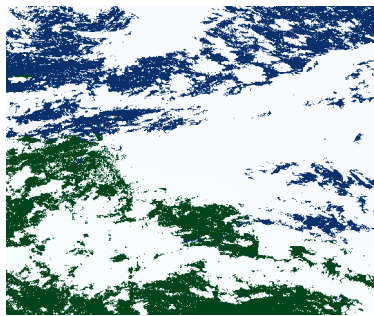
Satellite cloud coverage at 16:45



Numerical prediction at 16:45



Satellite cloud coverage at 9:15



Satellite cloud coverage at 19:45



Numerical prediction at 19:45

Fig. 14. Comparison of the persistence forecast from 9:15 (first column, same image repeated) and the numerical prediction (third column) with the cloud coverage product derived from GOES-13 satellite imagery at different times on May 26th, 2015 over French Guiana and other parts of South America. First row: at 10:45. Second row: at 13:45. Third row: at 16:45. Fourth row: at 19:45. The persistence forecast from 9:15UTC looks subjectively better than the model forecast for all the four cases.

- [13] A. Plaza, P. Martinez, J. Plaza, and R. Perez, "Dimensionality reduction and classification of hyperspectral image data using sequences of extended morphological transformations," *IEEE Trans. Geosci. Remote Sens.*, vol. 43, no. 3, pp. 466–479, 2005.
- [14] M. Fauvel, Y. Tarabalka, J. A. Benediktsson, J. Chanussot, and J. C. Tilton, "Advances in spectral-spatial classification of hyperspectral images," *Proc. IEEE*, vol. 101, no. 3, pp. 652–675, 2013.
- [15] K. Zhang, S.-C. Chen, D. Whitman, M.-L. Shyu, J. Yan, and C. Zhang, "A progressive morphological filter for removing nonground measurements from airborne LIDAR data," *IEEE Trans. Geosci. Remote Sens.*, vol. 41, no. 4, pp. 872–882, 2003.
- [16] M. Beauchemin, K. P. Thomson, and G. Edwards, "On the hausdorff distance used for the evaluation of segmentation results," *Can. J. Remote Sens.*, vol. 24, no. 1, pp. 3–8, 1998.
- [17] M.-P. Dubuisson and A. K. Jain, "A modified hausdorff distance for object matching," in *Pattern Recognition, Conference A: Computer Vision and Image Processing, Proceedings of the 12th IAPR International Conference on*, vol. 1, 1994, pp. 566–568.
- [18] V. Venugopal, S. Basu, and E. Foufoula-Georgiou, "A new metric for comparing precipitation patterns with an application to ensemble forecasts," *J. Geophys. Res.*, vol. 110, no. D8, 2005.
- [19] A. J. Baddeley, "An error metric for binary images," *Robust computer vision*, vol. 5978, 1992.
- [20] D. Ahijevych, E. Gilleland, B. G. Brown, and E. E. Ebert, "Application of spatial verification methods to idealized and NWP-gridded precipitation forecasts," *Weather Forecast.*, vol. 24, no. 6, pp. 1485–1497, 2009. [Online]. Available: <http://dx.doi.org/10.1175/2009WAF2222298.1>
- [21] J. Serra, *Image Analysis and Mathematical Morphology*. Orlando, FL, USA: Academic Press, Inc., 1983.
- [22] I. M. Mitchell, "The flexible, extensible and efficient toolbox of level set methods," *J. Sci. Comput.*, vol. 35, no. 2-3, pp. 300–329, 2008.
- [23] G. Brunet, S. Jones, and P. Rutii, Eds., *Seamless prediction of the Earth system: from minutes to months*. World Meteor. Org., 2015.
- [24] D. M. L. Sills, "On the MSC Forecasters Forums and the future role of the human forecaster," *Bull. Amer. Meteorol. Soc.*, vol. 90, pp. 619–627, 2009.
- [25] E. Gilleland, D. Ahijevych, B. G. Brown, B. Casati, and E. E. Ebert, "Intercomparison of spatial forecast verification methods," *Weather Forecast.*, vol. 24, pp. 1416–1430, 2009.
- [26] D. Sills, H. Yang, and P. Joe, "A lightning mapping array in southern Ontario, Canada: uses for severe weather nowcasting," in *Extended Abstracts, 27th AMS Conference on Severe Local Storms*, no. 83. Madison, WI: Amer. Meteorol. Soc., 2014.
- [27] J. Mailhot, J. Milbrandt, A. Giguère, R. McTaggart-Cowan, A. Erfani, B. Denis, A. Glazer, and M. Vallée, "An experimental high-resolution forecast system during the Vancouver 2010 Winter Olympic and Paralympic Games," *Pure Appl. Geophys.*, 2012.
- [28] W. Rison, R. J. Thomas, P. R. Krehbiel, T. Hamlin, and J. Harlin, "A GPS-based three-dimensional lightning mapping system: Initial observations in central new mexico," *Geophys. Res. Letters*, vol. 26, pp. 3573–3576, 1999.
- [29] E. W. McCaul, S. J. Goodman, K. M. LaCasse, and D. J. Cecil, "Forecasting lightning threat using cloud-resolving model simulations," *Weather Forecast.*, vol. 24, pp. 709–729, 2009.
- [30] D. Wilks, *Statistical Methods in the Atmospheric Sciences*, ser. Academic Press. Academic Press, 2011.
- [31] C. F. Mass, D. Ovens, K. Westrick, and B. A. Colle, "Does increasing horizontal resolution produce more skillful forecasts?" *Bull. Amer. Meteorol. Soc.*, vol. 83, no. 3, pp. 407–430, 2002.
- [32] E. Gilleland, "Spatial forecast verification: Baddeley's delta metric applied to the ICP test cases," *Weather Forecast.*, vol. 26, pp. 409–415, 2011.
- [33] A. M. Fridlind, A. S. Ackerman, A. Grandin, F. Dezitter, M. Weber, J. W. Strapp, A. V. Korolev, and C. R. Williams, "High ice water content at low radar reflectivity near deep convection. part I: Consistency of in situ and remote-sensing observations with stratiform rain column simulations," *Atmos. Chem. Phys.*, vol. 15, no. 20, pp. 11 713–11 728, 2015.
- [34] J. Côté, S. Gravel, A. Méthot, A. Patoine, M. Roch, and A. Staniforth, "The operational CMC-MRB global environmental multiscale (GEM) model. part I: Design considerations and formulation," *Mon. Weather Rev.*, vol. 126, no. 6, pp. 1373–1395, 1998.
- [35] J. A. Milbrandt and M. K. Yau, "A multimoment bulk microphysics parameterization. part II: A proposed three-moment closure and scheme description," *J. Atmos. Sci.*, vol. 62, no. 9, pp. 3065–3081, 2005.
- [36] A. K. Heidinger, A. T. Evan, M. J. Foster, and A. Walther, "A naive bayesian cloud-detection scheme derived from CALIPSO and applied within PATMOS-x," *J. Appl. Meteorol.*, vol. 51, no. 6, pp. 1129–1144, 2012.
- [37] B. Turner, I. Zawadzki, and U. Germann, "Predictability of precipitation from continental radar images. part III: Operational nowcasting implementation (MAPLE)," *J. Appl. Meteorol.*, vol. 43, no. 2, pp. 231–248, 2004.
- [38] C. Davis, B. Brown, and R. Bullock, "Object-Based Verification of Precipitation Forecasts. Part I: Methodology and Application to Mesoscale Rain Areas," *Mon. Wea. Rev.*, vol. 134, no. 7, pp. 1772–1784, 2006.
- [39] P. Passalacqua, T. Do Trung, E. Foufoula-Georgiou, G. Sapiro, and W. E. Dietrich, "A geometric framework for channel network extraction from lidar: Nonlinear diffusion and geodesic paths," *J. Geophys. Res. Earth Surf.*, vol. 115, no. F1, 2010.



Dominique Brunet received the B.Sc. and M.Sc. degrees in mathematics from the Université Laval, Québec City, Canada, in 2005 and 2007, respectively and the Ph.D. degree in Applied Mathematics, from the University of Waterloo, Waterloo, Canada, in 2012.

He is currently a Physical Scientist (Research) in the Cloud Physics and Severe Weather Research Section at Environment and Climate Change Canada in Toronto, ON, Canada. He was previously a Postdoctoral Fellow in Radiation Physics at the Princess Margaret Cancer Center working on image-guided radiation therapy. His research expertise includes image processing and image-quality assessment, with a focus on mathematical and statistical methods. His current research interests are spatial weather verification, shape processing and lightning data processing.

Dr. Brunet is a frequent reviewer of IEEE Transactions on Image Processing and has also reviewed in IET Image Processing, Journal of Hydrometeorology (AMS), Signal Processing (Elsevier), Applied Mathematical Modelling (Elsevier), Journal of Signal, Image and Video Processing (Springer), Statistics and Computing (Springer), Signal Processing: Image Communication (Elsevier), Information Sciences (Elsevier), Image and Vision Computing (Elsevier), and IEEE Signal Processing Letters.



David Sills earned a Ph.D. degree in atmospheric science from York University in Toronto, Canada, in 1998.

He has served as a Severe Weather Scientist at Environment and Climate Change Canada, Government of Canada, in Toronto since 1999. His main research interests are severe weather process science and climatology, particularly with respect to lightning and tornadoes, and the development of new prediction techniques. He has led or co-authored 24 journal publications and 31 conference papers.

Dr. Sills has served as a reviewer for Weather and Forecasting, Journal of Applied Meteorology and Climatology, Atmosphere-Ocean, Atmospheric Research, Atmospheric Environment, Boundary-Layer Meteorology, and Journal of Wind Engineering and Industrial Aerodynamics, among others.

He is a member of the Canadian Meteorological and Oceanographic Society and the American Meteorological Society.